

# Modified Gravity-GADGET: A new code for cosmological hydrodynamical simulations of modified gravity models

Ewald Puchwein<sup>1</sup>, Marco Baldi<sup>2,3</sup> and Volker Springel<sup>1,4</sup>

<sup>1</sup>*Heidelberger Institut für Theoretische Studien, Schloss-Wolfsbrunnengasse 35, 69118 Heidelberg, Germany*

<sup>2</sup>*Dipartimento di Fisica e Astronomia, Università di Bologna, Viale B. Pichat 6/2, 40127 Bologna, Italy*

<sup>3</sup>*INAF, Osservatorio Astronomico di Bologna, Via Ranzani 1, 40127 Bologna, Italy*

<sup>4</sup>*Zentrum für Astronomie der Universität Heidelberg, Astronomisches Recheninstitut, Mönchhofstr. 12-14, 69120 Heidelberg, Germany*

24 September 2018

## ABSTRACT

We present a new massively parallel code for N-body and cosmological hydrodynamical simulations of modified gravity models. The code employs a multigrid-accelerated Newton-Gauss-Seidel relaxation solver on an adaptive mesh to efficiently solve for perturbations in the scalar degree of freedom of the modified gravity model. As this new algorithm is implemented as a module for the P-GADGET3 code, it can at the same time follow the baryonic physics included in P-GADGET3, such as hydrodynamics, radiative cooling and star formation. We demonstrate that the code works reliably by applying it to simple test problems that can be solved analytically, as well as by comparing cosmological simulations to results from the literature. Using the new code, we perform the first non-radiative and radiative cosmological hydrodynamical simulations of an  $f(R)$ -gravity model. We also discuss the impact of AGN feedback on the matter power spectrum, as well as degeneracies between the influence of baryonic processes and modifications of gravity.

**Key words:** cosmology: theory – methods: numerical

## 1 INTRODUCTION

One of the most puzzling open issues in modern physics concerns the origin of the observed late-time accelerated expansion of the Universe (Riess et al. 1998; Perlmutter et al. 1999; Schmidt et al. 1998). This acceleration has no natural explanation in the framework of a cosmological model based on Einstein’s General Relativity and standard particle physics. Therefore, either new fields with exotic global properties (as, e.g., a negative effective pressure) or new physics in the gravity sector have to be invoked in order provide a consistent description of the cosmic evolution. The former approach is generally referred to as “Dark Energy” (DE, hereafter), while the latter goes under the name of “Modified Gravity” (MG).

More conservative explanations for the observed cosmic acceleration have also been attempted, for example as a backreaction effect of the formation of nonlinear cosmic structures on the background expansion of the universe (see e.g. Kolb et al. 2006; Rasanen 2011; Clarkson et al. 2011) or through the presence of a very large void surrounding the Milky Way’s location and mimicking a late-time accelerated expansion (see e.g. Mustapha et al. 1997; Tomita 2001; Wiltshire 2007). However, such possibilities have been claimed either to produce an insufficient effect on the cosmic evolution to account for the observed acceleration (see e.g.

Behrend et al. 2008; Green & Wald 2011; Baumann et al. 2012), or to be at odds with independent observational data (as shown e.g. by Zumalacarregui et al. 2012).

The presently accepted cosmological model (e.g. Ade et al. 2013) – where the accelerated expansion is driven by a cosmological constant  $\Lambda$  – represents the boundary between standard physics and the wide range of DE and MG extended scenarios. Any extension of particle physics or of General Relativity besides a cosmological constant necessarily introduces additional degrees of freedom that would indicate the incompleteness of one or both of these two pillars of modern physics. It is therefore not surprising that the detection of possible deviations from the expected behaviour of a cosmological constant has become a primary target for a number of large and challenging observational campaigns, such as e.g. PanStarrs (Kaiser et al. 2002), HETDEX (Hill et al. 2008), DES (Abbott et al. 2005), LSST (Ivezic et al. 2008) and Euclid<sup>1</sup> (Laureijs et al. 2011).

Moving beyond the boundary between standard and non-standard physics represented by the cosmological constant corresponds to opening a Pandora’s box in terms of possible alternative and competing theories (see e.g. Amendola et al. 2012, for a recent comprehensive review).

<sup>1</sup> [www.euclid-ec.org](http://www.euclid-ec.org)

These include a large number of different realisations of dynamical DE models, generally characterised by the cosmic evolution of a classical scalar field, as (just to cite the most popular) *Quintessence* (Wetterich 1988; Ratra & Peebles 1988), *k-essence* (Armendariz-Picon et al. 2001), *Phantom* (Caldwell 2002) and *Quintom* (Feng et al. 2005) DE scenarios, generally assuming negligible spatial perturbations and interactions of the DE scalar field. More sophisticated models can be obtained by dropping such assumptions and allowing the DE scalar field to cluster at sub-horizon scales and to have direct interactions with standard particles as for the case of *Clustering Dark Energy* (Creminelli et al. 2009; Sefusatti & Vernizzi 2011; Batista & Pace 2013) and *Coupled Quintessence* (Wetterich 1995; Amendola 2000; Farrar & Peebles 2004; Amendola et al. 2008; Baldi 2011). On the other hand, several possible modifications of General Relativity have also been proposed, including *Scalar-Tensor theories* of gravity (as e.g.  $f(R)$  models, Buchdahl 1970; Starobinsky 1980; Hu & Sawicki 2007; Sotiriou & Faraoni 2010), the *DGP* scenario (Dvali et al. 2000), or the *Galileon* model (Nicolis et al. 2009).

All these MG theories, however, need to rely on specific screening mechanisms capable of suppressing the deviations from the behaviour of standard gravity in the local environment of our Galaxy in order to comply with the very stringent observational tests of general relativity that have been performed on Earth and within the solar system (see e.g. Bertotti et al. 2003; Will 2005). Several possible ways to obtain an environment-dependent screening of the effects of a modified theory of gravity have been proposed in recent years, including the *Chameleon* (Khoury & Weltman 2004), the *Dilaton* (Gasperini et al. 2002), the *Symmetron* (Hinterbichler & Khoury 2010) or the *Vainshtein* (Vainshtein 1972; Deffayet et al. 2002) mechanisms. All such mechanisms are based on the development of large (i.e. possibly nonlinear) spatial perturbations of the new degrees of freedom associated to local matter overdensities, thereby recovering standard gravity in high-density environments such as in our Galaxy.

Due to such nonlinearities, a fully consistent description of these screening mechanisms and of their effects on structure formation needs to rely on numerical techniques, and in particular on suitable modifications of N-body algorithms capable of solving for the spatial modulation of the deviation from standard gravity along with the usual evolution of matter density perturbations (see Baldi 2012, for a recent review on the implementation of DE and MG models in N-body simulations). These requirements have led in the last years to the development of a few specifically-designed N-body codes for MG cosmologies, starting from the first  $f(R)$  algorithm realised by Oyaizu (2008) using a fixed-resolution particle-mesh approach, to more recent implementations exploiting Adaptive Mesh Refinement (AMR) techniques that were also extended to a wider variety of MG models with different types of screening mechanisms (see e.g. Khoury & Wyman 2009; Li et al. 2012b; Brax et al. 2011; Davis et al. 2012; Llinares & Mota 2013a). These various codes have been successfully employed to investigate different possible observational features of MG theories in the statistical and structural properties of collapsed CDM halos, as their impact on e.g. the matter power spectrum (see e.g. Oyaizu 2008; Schmidt et al. 2009; Li et al. 2012b), redshift-space

distortions (Jennings et al. 2012), geometrical and dynamical properties of virialized halos (Lombriser et al. 2012a; Lee et al. 2013; Lam et al. 2012; Llinares & Mota 2013b), or the statistics of CDM halos and voids (as in Zhao et al. 2010; Zhao et al. 2011; Winther et al. 2012; Li et al. 2012a). These numerical investigations have shown for a number of realisations of MG cosmologies that they can result in sizeable effects on, e.g., the matter power spectrum, the abundance of massive halos, or the large-scale velocity field, at length and mass scales that will become directly testable with the next generation of wide-field galaxy surveys, with a particular relevance for Euclid and LSST.

The same scales and mass ranges, however, appear to be heavily affected by a number of baryonic astrophysical processes (see e.g. Puchwein et al. 2005, 2008; Stanek et al. 2009; van Daalen et al. 2011; Semboloni et al. 2011; Casarini et al. 2011) that have not been fully understood yet and whose implementation in cosmological hydrodynamical simulations requires the development of effective recipes to reproduce the integrated effects of physical processes below the resolution limit. The implied degeneracy between the observational features of cosmological models for the accelerated expansion of the universe and astrophysical processes at small scales represents one of the most problematic aspects for a full exploitation of the wealth of high-quality data that will become available over the next decade. It is therefore particularly important to be able to quantify the level of this degeneracy, or in other words to be able to predict to which extent our assumptions on astrophysical processes at small scales can bias our conclusions on cosmological model selection, and vice versa. To this end, the possibility to combine, in a single cosmological simulation code, both the implementation of specific MG scenarios and state-of-the-art prescriptions for small-scale baryonic processes, like feedback from AGN, represents a crucial step in the development of a robust interpretative framework within which to process and analyse present and future data.

In this work, we present a new tool for cosmological N-body and hydrodynamical simulations, called MG-GADGET that was developed with the main goal of allowing such combined investigation of MG theories and baryonic effects. It is implemented as a module for the widely used Tree-PM SPH-code P-GADGET3 and therefore inherits its up to date implementations of gas cooling, star formation, supernova and AGN feedback mechanisms, that have been developed in the last years for this code. The MG solver is based on a Newton-Gauss-Seidel relaxation scheme with adaptive resolution and provides an efficient computation of the MG extra degrees of freedom. In the remainder of the paper, we will describe the specific MG scenarios that can be presently treated with our code (Sec. 2), we will discuss in detail the algorithm implemented in MG-GADGET for the MG solver (Sec. 3), as well as results of simple test problems to assess the accuracy of the code (Sec. 4). Then we will present the first cosmological simulations performed with MG-GADGET with a focus on the impact of MG on the matter power spectrum (Sec. 5) and the outcomes of some radiative and non-radiative hydrodynamical simulations of MG models (Sec. 6). Finally, in Sec. 7 we will summarize our results and draw our conclusions.

## 2 F(R)-GRAVITY

We will use  $f(R)$ -gravity models as a testbed and first application of our MG code. Such models are generalizations of Einstein's general relativity, i.e. the Ricci scalar  $R$  in the Einstein-Hilbert action is replaced by a function of  $R$ , or more precisely by  $R + f(R)$  in our notation. The action is then given by

$$S = \int d^4x \sqrt{-g} \left( \frac{R + f(R)}{16\pi G} + \mathcal{L}_m \right), \quad (1)$$

where  $G$  is the gravitational constant,  $\mathcal{L}_m$  is the Lagrangian density of matter and  $g$  is the determinant of the metric tensor. The field  $f_R \equiv \frac{df(R)}{dR}$  can be interpreted as a scalar degree of freedom of such models. For viable models with  $f_R \ll 1$  and in the quasistatic approximation, i.e. assuming  $|\nabla f_R| \gg \frac{\partial f_R}{\partial t}$ , the field equation for  $f_R$  is given by (see e.g. Oyaizu 2008)

$$\nabla^2 f_R = \frac{1}{3c^2} (\delta R - 8\pi G \delta\rho), \quad (2)$$

where we have here restored factors of the speed of light  $c$ , and  $\delta\rho$  and  $\delta R$  are the perturbations in the density and scalar curvature respectively. The gravitational potential  $\phi$  satisfies (Hu & Sawicki 2007)

$$\nabla^2 \phi = \frac{16\pi G}{3} \delta\rho - \frac{1}{6} \delta R. \quad (3)$$

In the model described by Hu & Sawicki (2007),  $f(R)$  is given by

$$f(R) = -m^2 \frac{c_1 \left(\frac{R}{m^2}\right)^n}{c_2 \left(\frac{R}{m^2}\right)^n + 1}, \quad (4)$$

where  $m^2 \equiv H_0^2 \Omega_m$ . Here,  $H_0$  is the present day Hubble parameter and  $\Omega_m$  is the mean matter density in units of the critical density of the Universe.  $n$ ,  $c_1$  and  $c_2$  are free parameters. When suitably chosen, this model exhibits the chameleon mechanism, so that standard general relativity theory is restored in massive objects, or more precisely within deep potential wells. A cosmic expansion history that is close to  $\Lambda$ CDM can be obtained if we require  $c_2(R/m^2)^n \gg 1$ .  $f(R)$  is then given by  $f(R) = -m^2 c_1/c_2 + O((m^2/R)^n)$ . Setting the zeroth order term  $-m^2 c_1/c_2$  equal to  $-2\Lambda$ , where  $\Lambda$  is the desired cosmological constant, then the model closely recovers the expansion history of  $\Lambda$ CDM. This can be rephrased in a relation between the parameters  $c_1$  and  $c_2$ , namely

$$\frac{c_1}{c_2} = 6 \frac{\Omega_\Lambda}{\Omega_m}, \quad (5)$$

where  $\Omega_\Lambda$  is the vacuum energy density in units of the critical energy density of the Universe. The field  $f_R = \frac{df(R)}{dR}$  takes the form

$$f_R = -n \frac{c_1 \left(\frac{R}{m^2}\right)^{n-1}}{\left[c_2 \left(\frac{R}{m^2}\right)^n + 1\right]^2}, \quad (6)$$

in this model. Again assuming  $c_2(R/m^2)^n \gg 1$ , this reduces to

$$f_R \approx -n \frac{c_1}{c_2} \left(\frac{m^2}{R}\right)^{n+1}. \quad (7)$$

In a Friedmann-Robertson-Walker universe the scalar

curvature is given by

$$\bar{R} = 12H^2 + 6 \frac{dH}{d \ln a} H, \quad (8)$$

where  $a$  is the scale factor and  $H \equiv \dot{a}/a$  is the Hubble function. For a flat  $\Lambda$ CDM expansion history this can be rewritten as

$$\bar{R}(a) = 3m^2 \left( a^{-3} + 4 \frac{\Omega_\Lambda}{\Omega_m} \right). \quad (9)$$

Evaluating this at  $a = 1$  and plugging the result into Eq. (7) yields an equation for  $\bar{f}_{R0}$ , the background value of  $f_R$  at  $z = 0$ . Fixing the value  $\bar{f}_{R0}$ , hence, results in a relation between  $c_1$  and  $c_2$ . Together with Eq. (5), this completely determines both  $c_1$  and  $c_2$ . It is, therefore, possible to parametrise  $f(R)$ -models of this type by  $n$  and  $\bar{f}_{R0}$  rather than by  $n$ ,  $c_1$  and  $c_2$ . We adopt this convention throughout the remainder of this paper. Furthermore, all the simulations we present here assume  $n = 1$ . In this case,  $\bar{f}_R(z)$  and  $\delta R$  are given by

$$\bar{f}_R(a) = \bar{f}_{R0} \left( \frac{\bar{R}_0}{\bar{R}(a)} \right)^2 = \bar{f}_{R0} \left( \frac{1 + 4 \frac{\Omega_\Lambda}{\Omega_m}}{a^{-3} + 4 \frac{\Omega_\Lambda}{\Omega_m}} \right)^2, \quad (10)$$

$$\delta R = \bar{R}(a) \left( \sqrt{\frac{\bar{f}_R(a)}{f_R}} - 1 \right). \quad (11)$$

Together with Eqs. (2) and (3), this defines the set of equations that we need to solve numerically for the force computation in our cosmological simulations. Once these equations are solved, the gravitational acceleration can be computed in the standard way from the gradient of the gravitational potential, i.e.  $\mathbf{a} = -\nabla\phi$ .

Alternatively, combining Eqs. (2) and (3) yields

$$\nabla^2 \phi = 4\pi G \delta\rho - \frac{c^2}{2} \nabla^2 f_R. \quad (12)$$

From this, it is straightforward to identify the modified gravity contribution to the gravitational acceleration. It is given by

$$\mathbf{a}_{MG} = \frac{c^2}{2} \nabla f_R. \quad (13)$$

and can, hence, be directly computed from  $f_R$ .

## 3 THE SIMULATION CODE

Our new fully parallel cosmological simulation code for modified gravity models MG-GADGET (Modified-Gravity-GADGET) is based on the TreePM-SPH simulation code P-GADGET3, an updated and significantly extended version of GADGET-2 (Springel 2005). In order to use the code to follow structure formation in modified gravity models, it was, obviously, necessary to significantly change P-GADGET3's gravity solver. All the changes we implemented are described in detail below.

### 3.1 Using the gravitational tree as an adaptively refined mesh

P-GADGET3 uses a long-range/short-range force splitting to calculate Newtonian gravitational forces (see Springel (2005) for full details). Long-range forces are computed with Fast

Fourier transform methods, while short-range forces are evaluated using a hierarchical octree (see also Barnes & Hut 1986). Such a scheme is called a tree particle-mesh (TreePM) gravity algorithm. On coarse tree levels, the nodes of this gravitational octree exactly tessellate the simulation volume. On fine tree levels, instead, the nodes are no longer space-filling but cover only high density regions. Depending on how exactly the tree is built, the leaf nodes may not even be space filling in these regions. However, by selecting nodes from different levels it is possible to obtain a mesh that exactly tessellates the whole simulation volume and has higher resolution in high-density regions. In other words, nodes can be chosen that define an adaptive mesh that refines on high-density regions. This adaptive mesh can then be used to compute and store any scalar degree of freedom that the modified gravity model under consideration has. In particular, we will use it in the following to solve Eq. (2) for  $f_R$ , as well as for storing the corresponding effective mass density (defined below in Eq. (31)). The methods used for solving for  $f_R$  on this adaptive mesh are conceptually similar to those employed by Li et al. (2012b). Full details will be given in Secs. 3.2 and 3.3.

To obtain the adaptive mesh, we start with the root node and recursively check all tree nodes whether they should be selected as AMR cells. The exact criteria for selecting a node are as follows:

- (i) the node is not part of a coarser level node that has already been chosen as an AMR cell,
- (ii) the node has less than 8 daughter nodes, i.e. the daughter nodes (if they exist at all) do not cover the volume of the node completely and therefore would not qualify as AMR cells themselves.

Using these criteria for a given tree yields the highest resolution adaptive mesh that is space-filling. This is, however, not necessarily the best choice as using cells that are much smaller than the gravitational softening may not make sense. We, therefore, allow to set a maximum tree level on which AMR cells may reside. Then, nodes that are on this level and satisfy the first of the above criteria are selected even if they have 8 daughter nodes. This maximum AMR level is typically chosen such that the side length of nodes on this level is somewhat smaller than the gravitational softening.

Above we have described how we select tree nodes as AMR cells, we have, however, not yet specified how the tree is built in the first place. P-GADGET3 constructs the gravitational tree by sequentially inserting particles into the tree. Whenever a leaf node has already another particle attached in the octant in which the new particle should be added a subnode is created in that octant. Both particles are then attached to the subnode (unless both particles also fall in the same octant of the subnode, in that case a sub-subnode needs to be created). In this way, a sparse memory-efficient octree is built. Nodes in this tree may have any number of subnodes between 0 and 8. The criteria specified above allow selecting nodes that define a space-filling adaptive mesh even from such a sparse tree. However, for unfavourable particle configurations the number of particles per AMR cell can become quite large (up to several hundred particles). In such cases, the code would then achieve a significantly worse resolution on the AMR grid compared to the particle distribution. To avoid this, one can add missing subnodes to AMR

nodes that contain many particles so that its daughter nodes qualify as AMR nodes themselves. While one could think of different criteria for adding subnodes, we used the most rigorous approach throughout the remainder of this paper, i.e. whenever a new subnode of some node is created, we also create the 7 other subnodes. Using this approach each AMR cell contains at most 8 particles and typically  $\lesssim 1$ .

Before we can start solving for any scalar degree of freedom, we have to assign masses to the AMR cells. We do this with the cloud-in-cell (CIC) scheme, i.e. we represent each simulation particle by a constant density cube and assign to each AMR cells that overlaps with the cube the fraction of the particle mass that corresponds to the overlapping fraction of the volume. To this end, the side length of the AMR node that the particle resides in is adopted as the side length of the cube. When applied in this way the CIC scheme can also be used in regions in which the AMR grid changes resolution. Once a CIC mass has been assigned to all AMR cells we also compute masses for all coarser cells by simply summing up the masses of their daughter cells.

### 3.2 Discretisation of the $f(\mathbf{R})$ -equations

Models that produce cosmic structures that are compatible with observations correspond to small negative values of  $\bar{f}_{R0}$ . It then follows by Eq. (10) that  $\bar{f}_R(a)$  is also negative for all  $a$ . Eq. (11) would then yield an unphysical imaginary  $\delta R$  if  $f_R$  would attain a positive value at some position. A physical solution for  $f_R$  should, instead, be negative everywhere and at all times.  $f_R$  may, however, reach values very close to zero. This is problematic when using an iterative numerical solver to find  $f_R$  as finite step sizes may at some point yield a positive  $f_R$  value. The resulting imaginary  $\delta R$  would then prevent us from continuing the iteration and, hence, make the code unstable.

Following Oyaizu (2008), we do not solve directly for  $f_R$  but introduce a new field  $u$  which we define by

$$u \equiv \ln \left( \frac{f_R}{\bar{f}_R(a)} \right), \quad (14)$$

so that

$$f_R = \bar{f}_R(a) \times e^u. \quad (15)$$

Using the field  $u$  does by construction not permit  $f_R$  to change its sign and therefore avoids the above mentioned stability issue. Using Eq. (11), Eq. (2) can then be rewritten in terms of  $u$  as

$$\nabla^2 e^u + \frac{1}{3c^2 \bar{f}_R(a)} \left[ \bar{R}(a) \left( 1 - e^{-\frac{u}{2}} \right) + 8\pi G \delta \rho \right] = 0. \quad (16)$$

In order to solve this equation for  $u$  on a grid, we need to discretise  $\nabla^2 e^u$ . We do this in the same way as in Oyaizu

(2008), i.e.

$$\begin{aligned}
 (\nabla^2 e^u)_{i,j,k} &= \frac{1}{h^2} [b_{i-\frac{1}{2},j,k} u_{i-1,j,k} + b_{i+\frac{1}{2},j,k} u_{i+1,j,k} \\
 &\quad - (b_{i-\frac{1}{2},j,k} + b_{i+\frac{1}{2},j,k}) u_{i,j,k}] \\
 &+ \frac{1}{h^2} [b_{i,j,j-\frac{1}{2},k} u_{i,j-1,k} + b_{i,j,j+\frac{1}{2},k} u_{i,j+1,k} \\
 &\quad - (b_{i,j,j-\frac{1}{2},k} + b_{i,j,j+\frac{1}{2},k}) u_{i,j,k}] \\
 &+ \frac{1}{h^2} [b_{i,j,k-\frac{1}{2}} u_{i,j,k-1} + b_{i,j,k+\frac{1}{2}} u_{i,j,k+1} \\
 &\quad - (b_{i,j,k-\frac{1}{2}} + b_{i,j,k+\frac{1}{2}}) u_{i,j,k}], \quad (17)
 \end{aligned}$$

where  $i, j, k$  are the cell indices in the  $x, y$ , and  $z$  directions, respectively.  $h$  is the physical side length of a cell and

$$b_{i-\frac{1}{2},j,k} \equiv \frac{1}{2} (e^{u_{i-1,j,k}} + e^{u_{i,j,k}}), \quad (18)$$

$$b_{i+\frac{1}{2},j,k} \equiv \frac{1}{2} (e^{u_{i,j,k}} + e^{u_{i+1,j,k}}). \quad (19)$$

The coefficients for the  $y$  and  $z$  directions, i.e.  $b_{i,j-\frac{1}{2},k}$ ,  $b_{i,j+\frac{1}{2},k}$ ,  $b_{i,j,k-\frac{1}{2}}$ , and  $b_{i,j,k+\frac{1}{2}}$ , are defined in an analogous way. We additionally define

$$\mathcal{L}_{i,j,k} \equiv (\nabla^2 e^u)_{i,j,k} + \frac{1}{3c^2 f_R(a)} \bar{R}(a) \left(1 - e^{-\frac{u_{i,j,k}}{2}}\right) \quad (20)$$

and

$$f_{i,j,k} \equiv \frac{1}{3c^2 f_R(a)} 8\pi G \left(\bar{\rho}(a) - \frac{m_{i,j,k}}{h^3}\right), \quad (21)$$

where  $m_{i,j,k}$  is the mass assigned to cell  $(i, j, k)$  and  $\bar{\rho}(a) = \bar{\rho}_0/a^3$  is the mean physical matter density as a function of the scale factor. This allows us to discretise Eq. (16) in the following form

$$\mathcal{L}_{i,j,k} = f_{i,j,k}. \quad (22)$$

In the next section we will describe how to iteratively solve this equation.

### 3.3 Iterative solver with multigrid acceleration

Because of its nonlinearity, standard FFT-based methods are not suitable for solving the field equation for  $u$ . Therefore, most previous works (e.g. Oyaizu 2008; Li et al. 2012b) resorted to iterative Newton-Gauss-Seidel relaxation schemes. We also follow this approach here. Starting with an initial guess  $u_{i,j,k}^0$ , we obtain a new, typically more accurate approximation of  $u$  by

$$u_{i,j,k}^{n+1} = u_{i,j,k}^n - \frac{\mathcal{L}_{i,j,k}^n - f_{i,j,k}}{\frac{d\mathcal{L}_{i,j,k}^n}{du_{i,j,k}^n}}. \quad (23)$$

To compute  $\mathcal{L}_{i,j,k}^n$  and its derivative we need the value of  $u$  in cell  $(i, j, k)$ , as well as in its six direct neighbours. In each iteration, we update the cells using a *red-black sweep*, i.e. using the three-dimensional equivalent of a chessboard pattern. In the first half-sweep all *red* cells and in the second all *black* cells are updated. In each half-sweep, a cell is, thus, only affected by its six direct neighbours. The effect of some source term, e.g. a point mass, on the approximate solution, therefore, only propagates by two cells per iteration. The number of iterations needed to converge to a solution is thus roughly proportional to the dimension of the grid. On large

grids this can make the convergence of the algorithm very slow.

A standard technique to achieve faster convergence is to use *multigrid* acceleration. This means that a hierarchy of grids with different resolutions is used. The basic concept is that the large scale structure of the solution can be found quickly on a coarse grid, so that the iterations on the finer grids only need to recover the small scale properties which requires much fewer iterations. We adopt this approach in our simulation code and use tree levels that are coarser than the AMR level for the multigrid acceleration employing the so-called *full approximation scheme* (Brandt 1977).

In order to use this technique, we need an algorithm to map an approximate solution  $u$  to the next coarser or finer tree level. For going to a coarser grid, also known as *restriction* and denoted by the operator  $\mathcal{R}$ , we set the  $u$  value of the parent node to the average value of the daughter cells. To map to finer levels, i.e. for the *prolongation* denoted by  $\mathcal{P}$ , we apply either *straight injection*, which means that the  $u$  value of the parent node is assigned to all its daughter cells, or we compute the  $u$  values using a linear reconstruction which is additionally based on the gradient of  $u$  in the centre of the parent cell.

The equation that needs to be solved for the multigrid acceleration on the coarser grids differs slightly from Eq. (22) (see also Oyaizu 2008; Li et al. 2012b). Assume that we want to solve for  $u$  on a grid with grid spacing  $h$ . In the following, we make the grid resolution explicit by using superscripts. We omit the cell indices for convenience. Thus, Eq. (22) can be rewritten as

$$\mathcal{L}^h(u^h) = f^h. \quad (24)$$

Now assume that we have an approximate solution  $\hat{u}^h$  which satisfies

$$\mathcal{L}^h(\hat{u}^h) = \hat{f}^h. \quad (25)$$

Combining these two equations then yields

$$\mathcal{L}^h(u^h) - \mathcal{L}^h(\hat{u}^h) = f^h - \hat{f}^h. \quad (26)$$

As a next step, we coarsen this equation in order to represent it on a grid with two times larger grid spacing. We do this as follows,

$$\mathcal{L}^{2h}(u^{2h}) = f^{2h}, \quad (27)$$

where

$$f^{2h} = \mathcal{L}^{2h}(\mathcal{R}\hat{u}^h) + \mathcal{R}(f^h - \hat{f}^h). \quad (28)$$

Eq. (27) has the same form as Eq. (24) and can thus be iteratively solved in a similar fashion. For this our code uses  $\mathcal{R}\hat{u}^h$  as an initial guess. Large-scale features in the solution will then be recovered much faster than on the fine grid. Once a better approximation  $\hat{u}^{2h}$  of  $u^{2h}$  is found, the correction to  $u$  can be mapped back to the fine grid by

$$\hat{u}^{h,\text{new}} = \hat{u}^h + \mathcal{P}(\hat{u}^{2h} - \mathcal{R}\hat{u}^h). \quad (29)$$

Note that applying this correction to  $\hat{u}^h$  rather than, e.g. using  $\hat{u}^{h,\text{new}} = \mathcal{P}\hat{u}^{2h}$  has two significant advantages. First, the small scale features in  $\hat{u}^h$  are preserved. And second, the effects of an inaccurate mapping between different levels are reduced. This can be most easily seen in the case in which  $\hat{u}^{2h} = \mathcal{R}\hat{u}^h$ , i.e. if the coarse solution is not changed. It then

directly follows from Eq. (29) that also the correction to the fine solution is exactly equal to zero in spite of an imperfect mapping between the two levels.

The individual steps the code takes for solving Eq. (22) in a full timestep are as follows:

- (i) It starts on the finest tree level that still covers the complete simulation volume.
- (ii) The solution  $u$  on this level from the previous timestep is used as an initial guess for the iterative solver.
- (iii) Using Eq. (23), the code performs  $n_{\text{pre-smooth}}$  red-black sweeps.
- (iv) The new  $u$  values found in this way are mapped to the next coarser level.
- (v) The code solves the coarse-grid problem (Eq. (27)). If the coarse-grid dimension is larger than  $4^3$ , this is again done using multigrid acceleration. Otherwise, the iterative Newton-Gauss-Seidel solver is directly employed.
- (vi) The change in the coarse grid solution is mapped back to the fine grid according to Eq. (29).
- (vii) The code performs  $n_{\text{post-smooth}}$  red-black sweeps.
- (viii) If  $|\mathcal{L}_{i,j,k} - f_{i,j,k}|$  is smaller than some threshold value  $R_{\text{thres}}$  for all  $(i, j, k)$ ,  $u$  is accepted as the solution for this tree level. Otherwise, steps (iii) to (viii) are repeated, i.e. another so-called *V-cycle* is performed.

We have now found a solution  $u$  on the finest level that covers the complete simulation box. The code then proceeds to the next finer level. The grid, there, typically consists of a number of patches and, by definition, has boundaries as it does not cover the whole volume. In the cells next to the boundary we define  $\mathcal{L}_{i,j,k}$  using *ghost* cells. More precisely we add an additional layer of such cells around each patch and compute their  $u$  values by applying the prolongation operation to their parent node. These ghost cells can then be used as neighbours for the cells next to the boundary such that  $\mathcal{L}_{i,j,k}$  is defined for them and the iterative solver can be applied. The ghost cells themselves are, however, not updated during the iteration and retain the  $u$  value that they were assigned based on their parent node. More precisely, the solver works on levels that do not cover the whole volume in the following way:

- (ix) The solution for  $u$  previously found on the coarser level is mapped to the current tree level and used as an initial guess for the iterative solver, as well as for setting the  $u$  values of the ghost cells.
- (x) Eq. (22) on this level is then again solved using multigrid acceleration, i.e. performing steps (iii) to (viii) for the current level.
- (xi) Once the solution has been found the code proceeds to the next finer level.
- (xii) Steps (ix) to (xi) are performed for each tree level down to the finest AMR level.

To summarize, our code solves Eq. (22) on the finest tree level that still covers the complete simulation volume, as well as on all finer levels that contain AMR cells. For each level convergence can be accelerated using the multigrid technique. The steps listed above give a good overview of how our code works, however, some details still need to be filled in.

When we apply multigrid acceleration to grids that cover only part of the simulation volume, we only want to

iteratively update those regions of the coarser grids that correspond to the same part of the simulation box. We, thus, have to map the boundaries of the fine level to the coarser levels. This is achieved by employing a mask function (see, e.g. Guillet & Teyssier (2011) for a detailed discussion on how to use mask functions for this purpose). In our code, the mask function is set to 1 in all cells on the level for which  $u$  is currently computed. The mask function on the coarser levels which are used for the multigrid acceleration is then obtained by averaging the values of the daughter cells. If a cell on the coarse grid does not have daughter cells a mask value of 0 is assigned to it. We then include all cells in the red-black sweeps that are performed for the multigrid acceleration that have a mask value larger than some threshold value  $m_{\text{thres}}$ . We found  $m_{\text{thres}} = 0.4$  to work well and to result in a fast convergence.

### 3.4 Accounting for effective masses in the TreePM gravity

Once we have computed  $f_R = \bar{f}_R(a) \times e^u$  for all AMR cells, we can either compute the modified gravity accelerations according to Eq. (13) or include the corresponding effective mass density in the Poisson equation for the gravitational potential.

Adopting the latter approach, we first rewrite Eq. (3) as

$$\nabla^2 \phi = 4\pi G (\delta\rho + \delta\rho_{\text{eff}}), \quad (30)$$

where  $\delta\rho_{\text{eff}}$  is defined by

$$\delta\rho_{\text{eff}} = \frac{1}{3}\delta\rho - \frac{1}{24\pi G}\delta R, \quad (31)$$

and  $\delta R$  is given by Eq. (11). These equations imply that the  $f(R)$  modifications of gravity can be described as arising from an “effective mass density”  $\delta\rho_{\text{eff}}$ . We can, thus, solve Eq. (30) using the very well tested and optimized TreePM-gravity algorithm that P-GADGET3 uses for standard Newtonian gravity. The only modification that is required is adding the effective mass density that we obtain from the solution for  $f_R$  to the standard matter density.

In a TreePM code the mass density enters the computation in two places, that is in the masses assigned to the tree nodes and the particle-mesh (PM) grid cells. From Eq. (31) we already know the additional effective mass terms for all tree nodes that are AMR cells. The centre of effective mass is assumed to be the cell centre in that case. For the parent nodes of AMR cells the effective mass is computed by simply summing up the effective masses of the daughter nodes. Their centres of effective mass are also computed in a straightforward manner based on the effective masses and centres of effective mass of the daughter cells. As effective masses can be either positive or negative the centre of effective mass can in rare cases fall outside the node. To avoid numerical inaccuracies due to this, we always open such nodes in the tree walk.

The tree force computation is then done in the following way:

- (i) If a node on the AMR level or on coarser levels can

be directly used<sup>2</sup>, the gravitational acceleration of the considered particle is updated including both the contributions from the real and effective masses of the tree node.

(ii) If an AMR node needs to be opened, the acceleration due to the AMR node's effective mass is directly applied, while the acceleration due to the real mass is computed based on the daughter nodes or on the particles contained in the tree node.

The latter scheme accommodates the fact that the effective mass is not defined below the AMR level.

For the long-range gravity, the effective mass of an AMR cell is distributed among all overlapping PM grid cells. The fraction assigned to an individual PM grid cell is simply given by the ratio of overlapping to total AMR cell volume.

#### 4 $F(R)$ -TEST PROBLEMS

Before applying our code to cosmological simulations, we want to make sure it works reliably for simple test problems. To this end, we will look at the  $f_R$ -fields of a point mass and a peaked one-dimensional density distribution.

##### 4.1 The $f_R$ -field of a point mass

For this test, we use essentially the same setup as in Li et al. (2012b). More precisely, we use a  $256h^{-1}\text{Mpc}$  box at  $z = 0$  covered by a uniform  $N^3 = 128^3$  grid. The density in the individual cells is given by

$$\delta\rho = -10^{-4} \times \bar{\rho} \quad (32)$$

for all cells except the cell where the point mass is placed. There  $\delta\rho$  is given by

$$\delta\rho = 10^{-4} \times (N^3 - 1) \times \bar{\rho}. \quad (33)$$

We then compute  $f_R$  using our iterative solver on this uniform grid. Figure 1 compares our numerical result to an analytic solution, which is, however, only valid in an intermediate radial range. The analytic calculation assumes that  $\delta f_R = f_R - \bar{f}_R$  is small compared to  $|\bar{f}_R|$  so that Eq. (11) can be linearised. Then Eq. (2) reduces to a screened Poisson equation and the solution for  $\delta f_R$  is given by a Yukawa potential

$$\delta f_R = \frac{2Gm}{3c^2} \frac{e^{-\lambda r}}{r}, \quad (34)$$

where

$$\lambda = \sqrt{\left. \frac{1}{3c^2} \frac{dR}{df_R} \right|_{f_R = \bar{f}_R}}, \quad (35)$$

and  $m = 10^{-4} \times (N^3 - 1) \times \bar{\rho} V_{\text{cell}}$  is the mass value of the point mass and  $V_{\text{cell}}$  is the volume of a single cell. This solution is not valid very close to the point mass where the assumed linearity breaks down. Furthermore it is also inaccurate at very large radii, as there finite box size effects become important. Note that the analytic derivation assumes vacuum boundary conditions while the numerical solver adopts periodic boundary conditions.

<sup>2</sup> By which we mean that it does not need to be opened according to the geometrical or relative tree opening criterion.

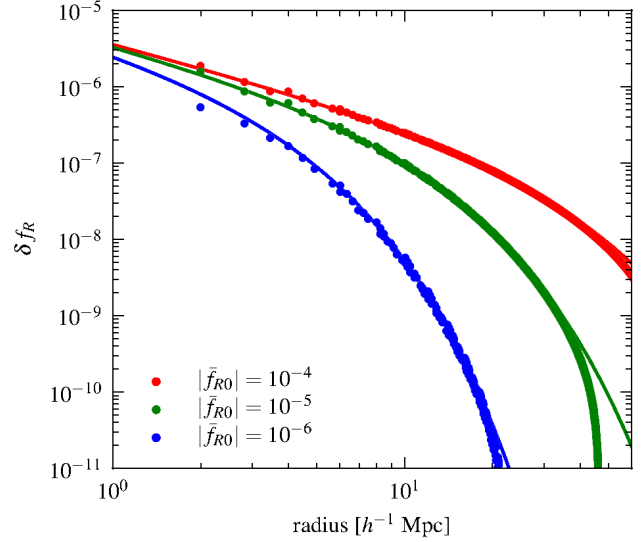


**Figure 1.** Solution for  $\delta f_R$  found by our code (circles) for a point mass for  $|\bar{f}_R| = 10^{-4}$ ,  $10^{-5}$  and a small spherical symmetric Gaussian mass distribution for  $|\bar{f}_R| = 10^{-6}$ . The solid lines indicate the analytic solutions of the linearised equation for  $\delta f_R$  assuming vacuum boundary conditions. They should be a good approximation of the full nonlinear solution with periodic boundary conditions in an intermediate radial range where non-linearities and box size effects are not important. In that radial range we find excellent agreement with the numerical results.

The figure displays results for different values of the background value  $\bar{f}_R$  of  $f_R$ . For  $|\bar{f}_R| = 10^{-4}$  and  $10^{-5}$  the assumed linearity still holds on the scale of the grid spacing. Thus the numerical results are in very good agreement with the analytic solution also at the smallest resolved radii. There is only a small amount of scatter around the analytic solution at  $r \lesssim 8 \text{Mpc}/h$ . This is, however, expected due to discretisation errors as this region is only a few times larger than the grid spacing. In an intermediate radial range there is almost perfect agreement between the analytic and numerical solution. At large radii, the solutions start to deviate from each other (most noticeably in the  $|\bar{f}_R| = 10^{-5}$  case) due to finite box size effects. This is completely expected and we checked that the deviation decreases when putting the same point mass in a larger box.

For  $|\bar{f}_R| = 10^{-6}$ , the analytic solution  $\delta f_R$  exceeds  $|\bar{f}_R|$  for  $r \lesssim 2 \text{Mpc}/h$ . This is unphysical as  $\delta R$  diverges for  $f_R \rightarrow 0$ . It is thus obvious that the assumed linearity no longer holds at small radii. Instead the Chameleon mechanism will start to screen  $f_R$  there. This can however not be resolved numerically for a point mass that resides only in a single cell. Therefore, for the  $|\bar{f}_R| = 10^{-6}$  case we have replaced the point mass by a small spherically symmetric Gaussian mass distribution  $\delta\rho \sim \exp[-r^2/(2 \text{Mpc}/h)^2]$  with the same total mass. Then the numerical result is in good agreement with the analytic solution for a true point mass except for the expected deviations at very small and very large radii.

Overall, these tests show that our numerical solver yields results that are in excellent agreement with the analytic solutions in the radial ranges in which the latter are valid. The deviations at very small and large radii are completely expected and are caused by assuming linearity and vacuum boundary conditions in the analytic derivation.

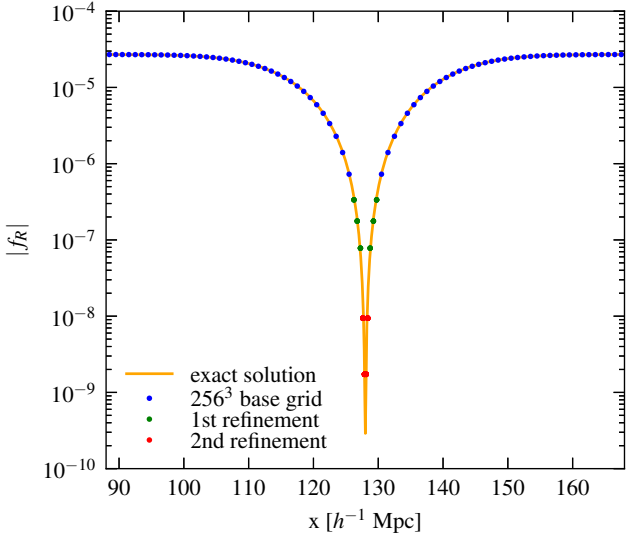


**Figure 2.** Solution for  $\delta f_R$  found by our AMR code (*circles*) for a 1D density peak and  $|\bar{f}_R| = 10^{-5}$ . The analytic solution is indicated by the *solid* line. The colours of the *circles* encode the refinement level of the individual AMR cells. The numerical solution on all AMR levels is in excellent agreement with the analytic prediction.

## 4.2 The $f_R$ -field of a 1D density peak

With the next test problem we want to check whether our solver also works reliably when using a mesh that adaptively refines on density peaks. To this end, we set up a 1D density peak in a  $256 h^{-1}\text{Mpc}$  box. More precisely we use a density field that depends only on the  $x$ -coordinate and has a peak at  $x = 128 h^{-1}\text{Mpc}$ . The shape of the peak is chosen such that it corresponds to the following  $f_R$  field

$$f_R = -A \times \left( 1 - \alpha e^{-\frac{\Delta x^2}{w^2}} \right), \quad (36)$$

where  $\Delta x$  is the distance from the density peak and  $w = 15 h^{-1}\text{Mpc}$ .  $\alpha = 0.99999$ , i.e. close to unity, was chosen to test our code deep in the nonlinear regime. We adopted  $|\bar{f}_R| = 10^{-5}$  for this test. The corresponding density perturbation is then given by

$$\delta\rho = \frac{1}{8\pi G} \left( \delta R(f_R) - 3c^2 \frac{d^2 f_R}{dx^2} \right) \quad (37)$$

according to Eq. (2), where  $\delta R(f_R)$  is given by Eq. (11). In this way it is easy to find an analytic expression for  $\delta\rho$ . We then choose  $A \approx 2.7 \times 10^{-5}$  such that the spatial average of  $\delta\rho$  vanishes. As a next step, we sample this density field with an adaptive grid with  $256^3$  base grid cells and two levels of refinement. This enables us to use it as an input to our adaptive-resolution multigrid-accelerated solver.

In Fig. 2, we display the solution which it finds for  $f_R$  and compare it to the analytic solution given by Eq. (36). They are in excellent agreement on the base grid, as well as on the refined grids. This demonstrates that our relaxation solver and the AMR algorithm work reliably for such a simple test problem. Further tests of our AMR code for the more realistic case of a cosmological density field are presented in Sec. 5.1.

## 5 COSMOLOGICAL $f(R)$ N-BODY SIMULATIONS

In the Hu & Sawicki (2007) model modifications of gravity appear only at low redshift. This can be understood from Eq. (10). At early times, i.e. for  $a \ll 1$ ,  $\bar{f}_R(a)$  is very small which essentially restores standard  $\Lambda\text{CDM}$ . We can, thus, start our cosmological  $f(R)$ -simulations from the same initial conditions that we use for  $\Lambda\text{CDM}$  runs. In the following we present further code tests and first results from full cosmological simulations performed with MG-GADGET.

### 5.1 Testing adaptive mesh refinement for a cosmological density field

In Sec. 4.2, we have tested our AMR algorithm by comparing its results to a known analytic solution. In more realistic situations in which an analytic solution is not known, it is in principle possible to validate the AMR method by comparison to results obtained on a very-high resolution fixed grid. In practice, however, obtaining a solution on a fixed grid with a resolution equal to the peak resolution of an AMR code may be computationally prohibitively expensive. To circumvent this problem, we perform such a comparison only for a single timestep and additionally limit the maximum refinement of the AMR code.

In Fig. 3, we compare the power spectrum of  $\delta\rho + \delta\rho_{\text{eff}}$ , where  $\delta\rho_{\text{eff}}$  is defined by Eq. (31), to the power spectrum of  $\delta\rho$  alone. The difference between the two can be interpreted as a measure of the enhancement of gravity as a function of scale. The comparison is based on a density field obtained from a full cosmological simulation at  $z = 0.5$ .  $f_R$  and  $\delta\rho_{\text{eff}}$  are computed for models which, at  $z = 0$ , have a background value of  $|\bar{f}_{R0}| = 10^{-5}$  and  $10^{-6}$ .  $f_R$  is found either on a low-resolution  $64^3$  or high-resolution  $512^3$  fixed grid or using the AMR method with a  $64^3$  base grid and a peak resolution equalling that of a  $512^3$  and a  $16384^3$  fixed grid. The refinement in the former AMR approach is thus restricted to yield the same peak resolution as the high-resolution fixed grid, while in the latter case the full AMR algorithm is employed.

For  $|\bar{f}_{R0}| = 10^{-5}$ , the restricted AMR computation is in almost perfect agreement with the results from the high-resolution fixed grid. This demonstrates that our AMR algorithm works well and recovers in a computationally much more efficient way the solution that one would obtain with a high-resolution fixed grid. As expected, using the full AMR algorithm results in an enhancement of gravity on even smaller spatial scales that can not be resolved by the high-resolution fixed grid. It is also worth noting that the low- and high-resolution fixed grid results are in excellent agreement with each other on scales  $k < 0.5 h/\text{Mpc}$ , which are well resolved on both grids.

For  $|\bar{f}_{R0}| = 10^{-6}$ , the restricted AMR computation is still in reasonably good agreement (better than  $\sim 12\%$  accuracy in the modification of gravity on well resolved scales  $k \lesssim 5 h/\text{Mpc}$ ) with the results obtained on the high-resolution fixed grid. There are, however, also noticeable deviations.

Interestingly, deviations of similar magnitude exist between the low- and high-resolution fixed grid calculations on large scales  $k < 0.5 h/\text{Mpc}$ , which are in principle well resolved on both grids. This can be understood in the follow-



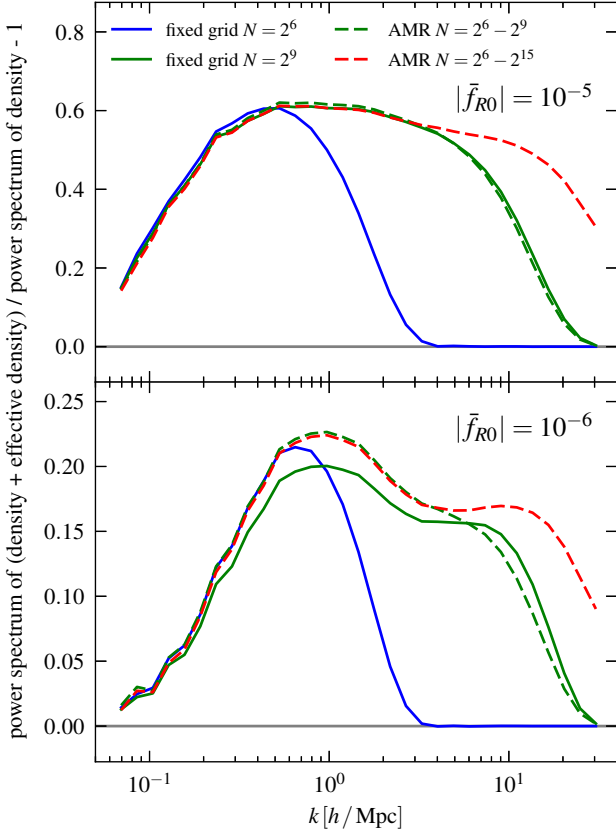


**Figure 3.** Enhancement of gravity as a function of scale. More precisely, we show the ratio of the power spectrum of  $\delta\rho + \delta\rho_{\text{eff}}$  to the power spectrum of  $\delta\rho$  for  $|\bar{f}_{R0}| = 10^{-5}$  (upper panel) and  $10^{-6}$  (lower panel) for a cosmological density field at  $z = 0.5$ . The effective density was computed for a co-moving  $100h^{-1}\text{Mpc}$  box either on a fixed grid or using the AMR technique. For the fixed grid results the grid resolution is quoted in the figure’s legend. For the AMR runs the base and peak resolutions are quoted. At the same peak resolution there is excellent agreement between high-resolution fixed grid and AMR runs for  $|\bar{f}_{R0}| = 10^{-5}$ . For  $|\bar{f}_{R0}| = 10^{-6}$  small deviations are visible which are due to fundamental limitations of the accuracy of *one-way interface* scheme AMR methods for very nonlinear problems. These discrepancies can, however, be alleviated by choosing a higher base resolution.

ing way. For  $|\bar{f}_{R0}| = 10^{-5}$ , the source term on the right-hand side of Eq. (2) is still rather linear in  $\delta f_R$ , so that coarse-graining Eq. (2) to the low-resolution grid does not significantly change the solution on large scales. For  $|\bar{f}_{R0}| = 10^{-6}$ , the source term is much more nonlinear which results in a slightly different coarse-grained solution. Physically, this most likely means that some of the objects in which the chameleon effect occurs are not properly resolved on the low-resolution grid, which somewhat changes the solution.

Like most other multigrid-accelerated AMR gravity solvers (including the RAMSES solver (Guillet & Teyssier 2011) on which the code presented in Li et al. (2012b) is based), our AMR algorithm uses a *one-way interface* scheme. This means that the solution on a coarse grid is used as a boundary condition for the refined patches on the next finer grid level, while the solution on the fine grid does not react back on the coarse grid solution in unrefined re-

gions. In particular, the solution that the AMR solver yields in regions that are only covered by the base grid is identical to the one which would be obtained on a fixed grid with the same resolution as the base grid. This is also the reason why the AMR runs yield the same results as the low-resolution fixed grid calculations on the largest scales. There, the deviations between the low- and high-resolution fixed grid runs for  $|\bar{f}_{R0}| = 10^{-6}$ , thus, necessarily result in deviations between the restricted AMR run and the high-resolution fixed grid results. This in turn means that there are fundamental limitations on the accuracy of *one-way interface* AMR schemes for very nonlinear equations.

Note, however, that for this test, we have chosen a rather low base resolution ( $\sim 1.5h^{-1}\text{Mpc}$  co-moving grid spacing) for the AMR runs. Using a higher base resolution, as done throughout the remainder of this paper alleviates this problem. Nevertheless, in the future, it may be worthwhile to develop a code which uses a *two-way interface* AMR scheme in which the fine grid solution acts back onto the coarse grid solution, e.g. by matching both  $f_R$  and its derivative at the coarse/fine-boundary, for strongly nonlinear models. For *one-way interface* AMR schemes we recommend using a relatively high base resolution to increase the accuracy for such models. Overall, our AMR scheme works extremely well for mildly nonlinear models and still very well for  $|\bar{f}_{R0}| = 10^{-6}$ , in particular when using a sufficiently fine base grid.

## 5.2 The matter power spectrum

The matter power spectrum is a sensitive and widely used statistics to describe structure formation in the Universe. In the context of modified gravity models it is, thus, one of the first quantities to investigate.

In Fig. 4, we display the enhancement of the matter power spectrum in the Hu & Sawicki (2007) model for  $n = 1$  and  $|\bar{f}_{R0}| = 10^{-4}$ ,  $10^{-5}$  and  $10^{-6}$ , compared to a standard  $\Lambda\text{CDM}$  universe. All runs were started from identical initial conditions at  $z = 100$ . The initial conditions are consistent with a WMAP-7yr cosmology (Komatsu et al. 2011), i.e.  $\Omega_M = 0.272$ ,  $\Omega_\Lambda = 0.728$ ,  $\Omega_B = 0.0456$ ,  $h = 0.704$ , and  $\sigma_8 = 0.809$ . A co-moving box size of  $200h^{-1}\text{Mpc}$ ,  $256^3$  particles, the same number of base grid cells and up to eight levels of refinement were used. Our results are compared to Li et al. (2012b).

In general, the power spectrum enhancements we find are in impressively good agreement with those obtained by Li et al. (2012b). This is quite reassuring. Minor deviations that do exist on small scales are not completely unexpected. First, we would like to point out that in this comparison cosmic variance does not appear on the largest scales but on intermediate and small scales. The reason for this is that the  $\Lambda\text{CDM}$  and modified gravity runs were started from identical initial conditions. Thus, on large scales in the linear regime, where mode-coupling is negligible, there is no cosmic variance as the initial phases and amplitudes are identical. On smaller scales, where mode-coupling becomes important, cosmic variance can appear because the enhancement of the amplitude of a particular mode depends on the amplitudes and phases of other modes. For our box size of only  $200h^{-1}\text{Mpc}$ , we do, thus, expect some cosmic variance on intermediate and small scales. In addition, there may be a mild

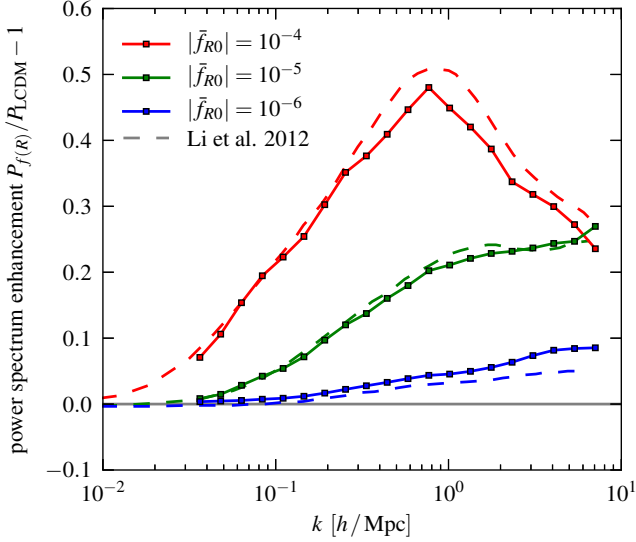


**Figure 4.** Matter power spectrum enhancements with respect to a standard  $\Lambda$ CDM model at  $z = 0$  for  $|\bar{f}_{R0}| = 10^{-4}$ ,  $10^{-5}$  and  $10^{-6}$  (solid lines and squares). Results obtained in  $1000 h^{-1}$  Mpc boxes by Li et al. (2012b) are shown for reference (dashed lines).

dependence on the resolution of the simulation as suggested by the discussion in Sec. 5.1. These deviations and effects are in agreement with the slightly different power spectrum enhancements obtained on small scales for simulations with different box sizes and resolutions in Li et al. (2012b) (see their Fig. 12). Overall, it is very reassuring that the power spectrum enhancements obtained with MG-GADGET are so strikingly similar to those found by Li et al. (2012b).

## 6 COSMOLOGICAL HYDRODYNAMICAL F(R) SIMULATIONS

So far almost all simulations of modified gravity models ignored the effects of baryonic physics. Here, we present the first – to our knowledge – non-radiative and radiative cosmological hydrodynamical simulations with modified gravity. In the following we discuss why such a simultaneous treatment of modified gravity and baryonic physics will be instrumental for successfully probing modifications of gravity with upcoming surveys like Euclid or LSST.

### 6.1 Degeneracies between baryonic physics and modifications of gravity

In Fig. 5, we compare the effects of modified gravity and baryonic physics on the total matter power spectrum. The green solid lines show the same power spectrum enhancements due to modified gravity as in Fig. 4, which were computed from collisionless simulations. The green dashed line displays the enhancement we obtain for a non-radiative hydrodynamical modified-gravity run of the same  $200 h^{-1}$  Mpc box with  $|\bar{f}_{R0}| = 10^{-5}$ . The hydrodynamics was followed with P-GADGET3’s entropy-conserving formulation of smoothed particle hydrodynamics (Springel & Hernquist 2002). As expected, the power spectrum enhancement in this non-radiative hydrodynamical simulation is very similar to

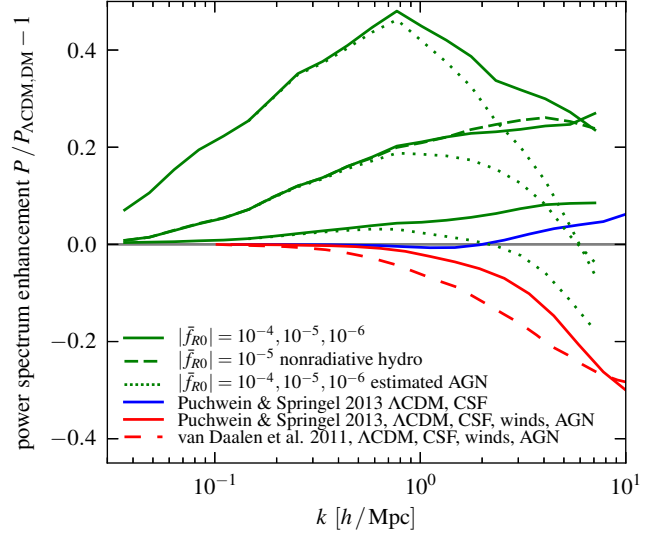


**Figure 5.** Comparison of the effects of modified gravity and baryonic physics on the total matter power spectrum at  $z = 0$ . All power spectrum enhancements are with respect to a collisionless  $\Lambda$ CDM simulation. AGN feedback affects the total matter power spectrum on similar scales as modified gravity. The magnitudes of the effects are also comparable. This illustrates that there are significant degeneracies between uncertainties in the baryonic physics and the impacts of modified gravity.

the one obtained in the collisionless run with the same  $f_{R0}$  value.

The blue solid line shows the effects of radiative cooling and star formation, which are treated using the Springel & Hernquist (2003) model, on the total matter power spectrum in a  $\Lambda$ CDM universe. The curve was obtained by comparing simulation *S13* from Puchwein & Springel (2013) to a collisionless simulation of the same box. In this run there is an increase of the total matter power spectrum on small scales due to the radiative collapse of baryons in halo centres, as well as the consequently triggered adiabatic contraction of the dark matter distribution. Note, however, that this simulation lacks an efficient feedback mechanism and therefore suffers from over-cooling.

The red solid line shows the effects of baryonic physics in  $\Lambda$ CDM simulations that in addition to radiative cooling and star formation account for supernovae-driven winds and energy injection by supermassive black holes, i.e. for active galactic nuclei (AGN) feedback which is treated essentially as in Sijacki et al. (2007)<sup>3</sup>. This model, which accounts for both quasar- and radio-mode AGN feedback, was shown to result in a self-regulated black hole growth (Di Matteo et al. 2005; Sijacki et al. 2007) and results in much more realistic properties of galaxy clusters (Puchwein et al. 2008) and their central galaxies (Puchwein et al. 2010), as well as abundances of massive galaxies (Puchwein & Springel 2013). The curve is based on a simulation with essentially the same parameters as the

<sup>3</sup> See Puchwein & Springel (2013) for details on minor modifications with respect to the AGN feedback model in Sijacki et al. (2007)

*S16* run from Puchwein & Springel (2013). The only difference is that a larger seed black hole mass of  $10^5 h^{-1} M_{\odot}$  was used, which results in a slightly better agreement of cluster and group properties with observations. As the power spectrum at Mpc scales is dominated by the one-halo term of these objects (e.g. Semboloni et al. 2011), this seems to be a better choice for the comparison presented here. It can clearly be seen that at least in this model AGN feedback significantly suppresses the total matter power spectrum on scales smaller than  $\sim 6 h^{-1}$  Mpc. This qualitatively confirms a similar finding by van Daalen et al. (2011). Their result is shown for comparison (*dashed red* line).

Given that the AGN feedback prescription in van Daalen et al. (2011) and Puchwein & Springel (2013) are partly based on the same assumptions, i.e. an accretion model motivated by Bondi-Hoyle-Lyttleton accretion and thermal injection of the feedback energy, the difference between these results should probably be considered as a lower limit of the theoretical uncertainty of the impact of AGN feedback. Understanding these baryonic effects on the total matter power spectrum and their uncertainties will be of utmost importance for fully exploiting surveys like Euclid or LSST that aim to probe cosmology by weak lensing (e.g. Semboloni et al. 2011). These results suggest that, ultimately, the smallest spatial scales that can be used for such studies may be determined by our (limited) understanding of baryonic physics.

If, for the moment, we boldly assume that the relative suppression of the total matter power spectrum by baryonic physics, most notably by AGN feedback, is the same in modified gravity as in the  $\Lambda$ CDM simulations from Puchwein & Springel (2013), we obtain the *green dotted* curves which show the expected power in modified gravity models when accounting for all the aforementioned baryonic physics. These results illustrate that baryonic physics and modified gravity affect the matter distribution on similar scales. Especially for the  $|\tilde{f}_{R0}| = 10^{-6}$  model, also the magnitudes of the effects are very similar. Furthermore, the  $|\tilde{f}_{R0}| = 10^{-4}$  and  $10^{-5}$  models are already in tension with observational constraints on the scales of galaxies and smaller (see, e.g. Fig. 9 in Lombriser et al. (2012b) for an overview of observational constraints).

This comparison, therefore, shows that there are significant degeneracies between the effects of uncertain baryonic physics and modifications of gravity for models that are fully consistent with the data. Simulations that include both effects will, hence, be required for studying these degeneracies and for looking for signatures of modified gravity that are least affected by uncertainties in the baryonic physics.

The current version of MG-GADGET does in principle allow following the dynamical evolution in modified gravity models and processes like AGN feedback at the same time. However, such simulations require large volumes for covering all the scales in which we are interested and for reducing cosmic variance, as well as high resolution, so that the sub-resolution feedback model yields converged results. We, therefore, plan to put some more effort in further improving the code performance in situations with a high dynamic range before embarking on such an endeavour. As a first step in this direction, we have performed radiative cosmological hydrodynamical simulations with modified gravity

and a strongly simplified treatment of star formation. We present them below.

## 6.2 Radiative hydrodynamical simulations with $f(R)$ -gravity

Using MG-GADGET we performed the first radiative cosmological hydrodynamical simulations with  $f(R)$ -gravity. Radiative cooling and photoheating was included under the assumptions of a primordial gas decomposition and of ionisation equilibrium in the presence of an external UV background field as in Katz et al. (1996). Star formation was followed with a strongly simplified treatment (Viel et al. 2004) in which all gas particles exceeding a density of 1000 times the mean baryon density and having a temperature lower than  $10^5$  K are transformed into collisionless star particles. While this scheme may not produce realistic galaxy populations, it does allow obtaining reliable predictions for the intergalactic medium (IGM). For these simulations a comoving box size of  $40 h^{-1}$  Mpc, an initial particle number of  $2 \times 256^3$  (half of them gas and half of them dark matter),  $256^3$  base grid cells and up to eight levels of refinement were used.

Fig. 6 shows the volume-weighted probability distribution functions (PDFs) of the temperature and density of the intergalactic medium at  $z = 2$ . Differences between the  $\Lambda$ CDM and the modified gravity runs are visible in both PDFs. The effects on the temperature PDF, e.g. the 15% shift in the peak temperature, may, however, be rather small compared to uncertainties in the heating efficiency due to helium II reionization (see e.g. McQuinn et al. 2009) or the effects of a recently suggested additional heating of the IGM by TeV-blazars (Broderick et al. 2012; Puchwein et al. 2012).

In contrast, the effect of modified gravity on the gas density PDF is most likely much less degenerate with baryonic processes. The enhancement of gravity in the  $f(R)$  runs accelerates structure formation and results in voids that are emptier than in  $\Lambda$ CDM, as well as in a larger fraction of dense regions, although the latter is somewhat hard to see in the figure.

These effects on the IGM density distribution may have observable signatures in the Lyman- $\alpha$  forest. For example, the enhancement of the matter power spectrum may be reflected by a change in the Lyman- $\alpha$  forest transmitted flux power spectrum. It will be interesting to investigate this in more detail in the future.

## 7 SUMMARY AND CONCLUSIONS

We have presented the novel simulation code MG-GADGET which is well suited for performing large cosmological N-body and hydrodynamical simulations of modified gravity models. The code is massively parallel and uses a multigrid-accelerated relaxation scheme on an adaptively-refined mesh to solve for perturbations in the scalar degree of freedom of the considered modified gravity model. The code is implemented as a module for the widely used cosmological simulation code P-GADGET3. This allows us to account at the same time for baryonic processes like hydrodynamics or radiative cooling that P-GADGET3 is able to follow.

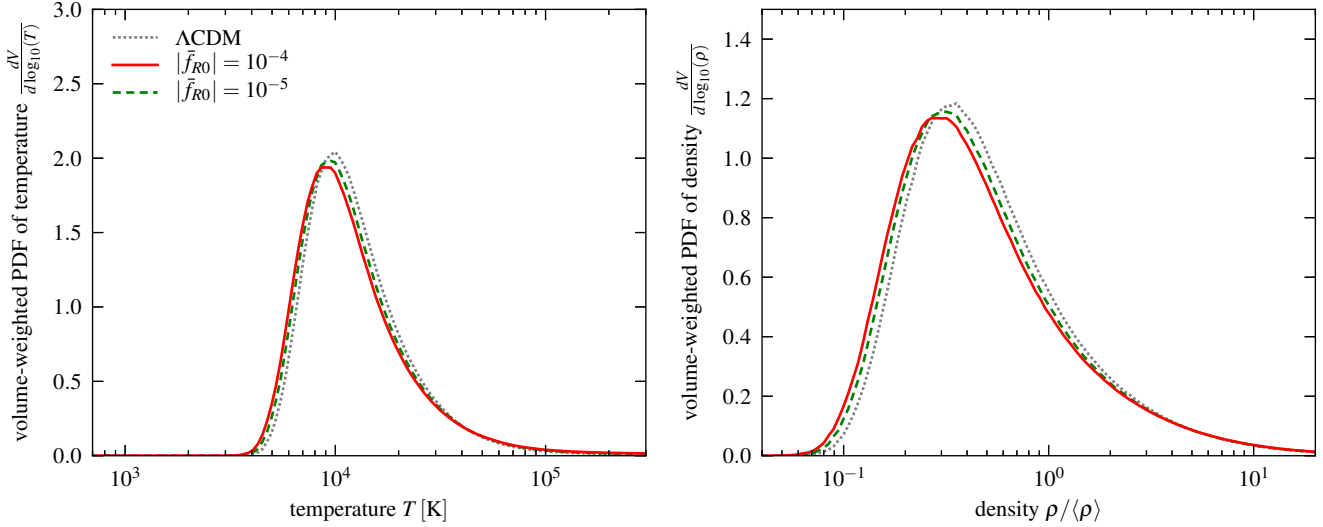


**Figure 6.** Volume-weighted PDF of gas temperature (*left panel*) and density (*right panel*) of the intergalactic medium in simulations with a standard  $\Lambda$ CDM cosmology and for modified gravity runs with  $|\bar{f}_{R0}| = 10^{-4}$  and  $10^{-5}$  at redshift  $z = 2$ .

As a first application we consider the chameleon-type  $f(R)$ -gravity model introduced by Hu & Sawicki (2007). Before performing full cosmological runs, we apply the code to a few simple test problems to assess the accuracy of the modified gravity solver. For a single point mass, the numerical results are in very good agreement with the analytic prediction in the radial range in which the latter is valid. The code also accurately recovers the analytic solution for the scalar degree of freedom in the case of a 1D density peak. For this test, we use adaptive refinement. The numerical and analytic solutions are in excellent agreement both on the base grid, as well as on the refined grids, thereby demonstrating that our AMR scheme works well.

We also test the AMR method under more realistic conditions, i.e. for a cosmological density field. Overall, it performs very well. For  $|\bar{f}_{R0}| = 10^{-5}$ , it yields essentially the same result as obtained on an extremely fine fixed grid with a resolution equalling the peak resolution of the adaptive mesh. However, this test also reveals fundamental limitations of the accuracy of *one-way* interface scheme AMR methods for very nonlinear equations. For the considered  $f(R)$ -gravity model strong nonlinearities occur for small  $|\bar{f}_{R0}|$  values. For  $|\bar{f}_{R0}| = 10^{-6}$ , small deviations between the extremely fine fixed grid and AMR solutions become noticeable. This discrepancy can, however, be alleviated by using a higher base grid resolution.

As a next step, we perform full cosmological  $f(R)$ -gravity N-body simulations and compare them to a reference  $\Lambda$ CDM run. We find scale-dependent enhancements of the matter power spectrum due to the modifications of gravity which are in very good agreement with results obtained by Li et al. (2012b). This concordance of different modified-gravity simulation codes is quite reassuring.

We then confront the effects of baryonic processes, like AGN feedback, on the total matter power spectrum with its changes due to modifications of gravity. It turns out that for those modified gravity models that are not in tension with observational constraints, both effects have similar magnitude and happen at similar spatial scales. This clearly

demonstrates that there are significant degeneracies between modified gravity and uncertainties in the baryonic physics. We hence require simulations that follow both processes at the same time to look for observational signatures of modified gravity that are least affected by such uncertainties.

For the aforementioned comparison, we have analysed the effects of AGN feedback on the total matter power spectrum in cosmological hydrodynamical  $\Lambda$ CDM simulations by Puchwein & Springel (2013). Our results confirm the finding of van Daalen et al. (2011) that AGN feedback significantly suppresses the total matter power spectrum on scales up to several Mpc. Understanding and accounting for this will be of utmost importance for fully exploiting upcoming surveys like Euclid or LSST that aim to probe cosmology by weak lensing (e.g. Semboloni et al. 2011). Given these results, it seems likely that the smallest spatial scale that can be used for such studies will ultimately be set by our knowledge or lack of knowledge of baryonic processes like feedback from AGN.

Finally, as a step towards simulations that account for modified gravity and complex baryonic physics at the same time, we perform the first – to our knowledge – modified gravity cosmological hydrodynamical simulations. Some of our runs also account for radiative cooling in the presence of an external UV background. In the latter runs, we find that modified gravity changes the density and temperature PDFs of the intergalactic medium. It will be interesting to explore in a future work whether this results in an observable signature of modified gravity in the Lyman- $\alpha$  forest.

## ACKNOWLEDGEMENTS

We are grateful to Luca Amendola and Jochen Weller for illuminating discussions. E.P. would also like to thank Rüdiger Pakmor, Andreas Bauer and Christoph Pfrommer for many helpful conversations. E.P. acknowledges support by the DFG through Transregio 33. M.B. is supported by the Marie Curie Intra European Fellowship “SIDUN” within the

7th Framework Programme of the European Community. MB also acknowledges partial support by the DFG Cluster of Excellence “Origin and Structure of the Universe” and by the TRR33 Transregio Collaborative Research Network on the “Dark Universe”. V.S. acknowledges support through SFB 881, ‘The Milky Way System’, of the DFG.

## REFERENCES

- Abbott T., et al., 2005, arXiv:astro-ph/0510346  
Ade P., et al., 2013, arXiv:1303.5076  
Amendola L., 2000, Phys. Rev. D, 62, 043511  
Amendola L. et al., 2012, arXiv:1206.1225  
Amendola L., Baldi M., Wetterich C., 2008, Phys. Rev. D, 78, 023015  
Armendariz-Picon C., Mukhanov V. F., Steinhardt P. J., 2001, Phys. Rev. D, 63, 103510  
Baldi M., 2011, MNRAS, 411, 1077  
Baldi M., 2012, Phys. Dark Univ., 1, 162  
Barnes J., Hut P., 1986, Nature, 324, 446  
Batista R., Pace F., 2013, arXiv:1303.0414  
Baumann D., Nicolis A., Senatore L., Zaldarriaga M., 2012, JCAP, 1207, 051  
Behrend J., Brown I. A., Robbers G., 2008, JCAP, 0801, 013  
Bertotti B., Iess L., Tortora P., 2003, Nature, 425, 374  
Brandt A., 1977, Mathematics of Computation, 31, 333  
Brax P., van de Bruck C., Davis A.-C., Li B., Shaw D. J., 2011, Phys. Rev. D, 83, 104026  
Broderick A. E., Chang P., Pfrommer C., 2012, ApJ, 752, 22  
Buchdahl H. A., 1970, MNRAS, 150, 1  
Caldwell R., 2002, Physics Letters B, 545, 23  
Casarini L., Macciò A. V., Bonometto S. A., Stinson G. S., 2011, MNRAS, 412, 911  
Clarkson C., Ellis G., Larena J., Umeh O., 2011, Rept. Prog. Phys., 74, 112901  
Creminelli P., D’Amico G., Norena J., Vernizzi F., 2009, JCAP, 0902, 018  
Davis A.-C., Li B., Mota D. F., Winther H. A., 2012, ApJ, 748, 61  
Deffayet C., Dvali G., Gabadadze G., Vainshtein A. I., 2002, Phys. Rev. D, 65, 044026  
Di Matteo T., Springel V., Hernquist L., 2005, Nature, 433, 604  
Dvali G., Gabadadze G., Porrati M., 2000, Physics Letters B, 485, 208  
Farrar G. R., Peebles P. J. E., 2004, ApJ, 604, 1  
Feng B., Wang X.-L., Zhang X.-M., 2005, Physics Letters B, 607, 35  
Gasperini M., Piazza F., Veneziano G., 2002, Phys. Rev. D, 65, 023508  
Green S. R., Wald R. M., 2011, Phys. Rev. D, 83, 084020  
Guillet T., Teyssier R., 2011, Journal of Computational Physics, 230, 4756  
Hill G. J., et al., 2008, ASP Conf. Ser., 399, 115  
Hinterbichler K., Khoury J., 2010, Phys. Rev. Lett., 104, 231301  
Hu W., Sawicki I., 2007, Phys. Rev. D, 76, 064004  
Ivezic Z., et al., 2008, arXiv:0805.2366  
Jennings E., Baugh C. M., Li B., Zhao G.-B., Koyama K., 2012, MNRAS, 425, 2128  
Kaiser N., et al., 2002, Proc. SPIE Int. Soc. Opt. Eng., 4836, 154  
Katz N., Weinberg D. H., Hernquist L., 1996, ApJS, 105, 19  
Khoury J., Weltman A., 2004, Phys. Rev. D, 69, 044026  
Khoury J., Wyman M., 2009, Phys. Rev. D, 80, 064023  
Kolb E. W., Matarrese S., Riotto A., 2006, New J. Phys., 8, 322  
Komatsu E., et al., 2011, ApJS, 192, 18  
Lam T. Y., Nishimichi T., Schmidt F., Takada M., 2012, Phys. Rev. Lett., 109, 051301  
Laureijs R. et al., 2011, arXiv:1110.3193  
Lee J., Zhao G.-B., Li B., Koyama K., 2013, ApJ, 763, 28  
Li B., Zhao G.-B., Koyama K., 2012a, MNRAS, 421, 3481  
Li B., Zhao G.-B., Teyssier R., Koyama K., 2012b, JCAP, 1, 51  
Llinares C., Mota D. F., 2013a, Phys. Rev. Lett., 110, 161101  
Llinares C., Mota D. F., 2013b, Phys. Rev. Lett., 110, 151104  
Lombriser L., Koyama K., Zhao G.-B., Li B., 2012a, Phys. Rev. D, 85, 124054  
Lombriser L., Schmidt F., Baldauf T., Mandelbaum R., Seljak U., Smith R. E., 2012b, Phys. Rev. D, 85, 102001  
McQuinn M., Lidz A., Zaldarriaga M., Hernquist L., Hopkins P. F., Dutta S., Faucher-Giguère C.-A., 2009, ApJ, 694, 842  
Mustapha N., Hellaby C., Ellis G., 1997, MNRAS, 292, 817  
Nicolis A., Rattazzi R., Trincherini E., 2009, Phys. Rev. D, 79, 064036  
Oyaizu H., 2008, Phys. Rev. D, 78, 123523  
Perlmutter S., et al., 1999, ApJ, 517, 565  
Puchwein E., Bartelmann M., Dolag K., Meneghetti M., 2005, A&A, 442, 405  
Puchwein E., Pfrommer C., Springel V., Broderick A. E., Chang P., 2012, MNRAS, 423, 149  
Puchwein E., Sijacki D., Springel V., 2008, ApJ, 687, L53  
Puchwein E., Springel V., 2013, MNRAS, 428, 2966  
Puchwein E., Springel V., Sijacki D., Dolag K., 2010, MNRAS, 406, 936  
Rasanen S., 2011, Class. Quant. Grav., 28, 164008  
Ratra B., Peebles P. J. E., 1988, Phys. Rev. D, 37, 3406  
Riess A. G., et al., 1998, AJ, 116, 1009  
Schmidt B. P., et al., 1998, ApJ, 507, 46  
Schmidt F., Lima M. V., Oyaizu H., Hu W., 2009, Phys. Rev. D, 79, 083518  
Sefusatti E., Vernizzi F., 2011, JCAP, 1103, 047  
Semboloni E., Hoekstra H., Schaye J., van Daalen M. P., McCarthy I. G., 2011, MNRAS, 417, 2020  
Sijacki D., Springel V., di Matteo T., Hernquist L., 2007, MNRAS, 380, 877  
Sotiriou T. P., Faraoni V., 2010, Rev. Mod. Phys., 82, 451  
Springel V., 2005, MNRAS, 364, 1105  
Springel V., Hernquist L., 2002, MNRAS, 333, 649  
Springel V., Hernquist L., 2003, MNRAS, 339, 289  
Stanek R., Rudd D., Evrard A. E., 2009, MNRAS, 394, L11  
Starobinsky A. A., 1980, Physics Letters B, 91, 99  
Tomita K., 2001, MNRAS, 326, 287  
Vainshtein A., 1972, Physics Letters B, 39, 393

- van Daalen M. P., Schaye J., Booth C. M., Dalla Vecchia C., 2011, MNRAS, 415, 3649  
Viel M., Haehnelt M. G., Springel V., 2004, MNRAS, 354, 684  
Wetterich C., 1988, Nuclear Physics B, 302, 668  
Wetterich C., 1995, A&A, 301, 321  
Will C. M., 2005, Living Rev. Rel., 9, 3  
Wiltshire D. L., 2007, arXiv:0712.3984  
Winther H. A., Mota D. F., Li B., 2012, ApJ, 756, 166  
Zhao G.-B., Li B., Koyama K., 2011, Phys. Rev. D, 83, 044007  
Zhao H., Macciò A. V., Li B., Hoekstra H., Feix M., 2010, ApJ, 712, L179  
Zumalacarregui M., Garcia-Bellido J., Ruiz-Lapuente P., 2012, JCAP, 1210, 009